



Study of Impact Load Directions on Tunnel Stability in a Cracked Rock Mass

Peng Ying¹ · Yu Ying⁵ · Fei Wu³ · Xiaohan Li⁴ · Ruihe Zhou² · Zheming Zhu³ · Lei Zhou³ · Xibin Li¹

Received: 29 November 2023 / Accepted: 7 August 2024

© The Author(s), under exclusive licence to Springer-Verlag GmbH Austria, part of Springer Nature 2024

Abstract

During tunnel construction and service, the rock surrounding tunnel is often subjected to multiple factors that influence its behaviour, such as dynamic disturbances (explosions, mechanical excavations, etc.) and existing cracks. These factors can readily induce safety issues, such as rock bursts and collapses. To investigate the effect of the loading direction on the failure modes of fractured tunnels, this study numerically investigated the destructive behaviour of tunnel models under the coupling effect of dynamic disturbance loads and external cracks using the finite-difference method (FDM). Additionally, a physical tunnel model with prefabricated cracks was created using green sandstone. A drop weight impact testing device (DWITD) was employed as the dynamic disturbance loading apparatus, while the relative azimuth angle between the tunnel and the cracks was varied. The crack initiation, arrest time, and extension rate were obtained using a crack fracture tester (CFT). The research results indicated that the preexisting cracks propagated continuously and eventually connected with the tunnel on the incident side under impact loads. The failure area of the tunnel was primarily controlled by the loading direction, exhibiting different modes of failure, often occurring at the bottom and arch of the tunnel. New cracks on the transmitted side of the tunnel appeared at different locations for different impact angles. The presence of cracks around the tunnel had a significant impact on the dynamic stress concentration factor (DSCF) of the rock surrounding the tunnel. The findings of this research can provide valuable guidance for tunnel stability analysis and the optimization of support schemes.

Highlights

- Crack parameter test was applied in crack propagation speed calculation.
- A large specimen with tunnel was used to calculate rock dynamic fracture toughness.
- The displacement trend line diagram was used to identify the fracture pattern of the crack under impact.
- The fracture toughness of rock is calculated by experimental numerical method.
- Stress wave and fracture mechanics theories were used to explain the interaction mechanism between cracks and tunnel.

Keywords Crack extension speed · Tunnel · Crack initiation time · Dynamic stress concentration factor · Crack initiation toughness

✉ Zheming Zhu
zhuzheming@scu.edu.cn

✉ Lei Zhou
zhouleitkx@126.com; zhuzheming@scu.edu.cn

¹ School of Landscape Architecture, Zhejiang A and F University, Hangzhou 311300, China

² School of Civil Engineering and Architecture, Anhui University of Technology, Ma'anshan 243002, China

³ State Key Laboratory for the Coal Mine Disaster Dynamics and Controls, Chongqing University, Chongqing 400044, China

⁴ State Key Laboratory of Hydraulics and Mountain River Engineering, School of Architecture and Environment, Sichuan University, Chengdu 610065, China

⁵ College of Mathematics and Physics, Chengdu University of Technology, Chengdu 610059, China

1 Introduction

many fragile surfaces, such as cracks and faults which may seriously affect the stability of underground structures (Zhu et al. 2015). In addition, the process of excavating tunnels will also face disturbances from dynamic loads originating from different directions. These dynamic loads can cause cracks to form and propagate around the tunnel, leading to tunnel damage and posing a significant risk to employee safety and economic feasibility. Due to the different directions of impact loads, the failure mode and degree of the tunnel may also change. Therefore, understanding how tunnel cracks respond to the impact of different directions of impact is vital for ensuring support design and construction safety.

In recent years, scientists have studied rock fragmentation through theoretical, experimental, and numerical simulations. To perform analyses, Fraldi et al. (Fraldi and Guaracino 2010) proposed a theoretical solution for the tunnel collapse of tunnels with any cross-section. Gong et al. (Gong et al. 2019) and Luo et al. (Luo et al. 2019) conducted experiments to simulate and study the spalling failure process of rectangular and D-shaped tunnels under different three-dimensional stress conditions. Saiang et al. analyze field-acquired data and predicted the damage zone and mechanical parameters near tunnel excavations using the methods of artificial neural networks (Malmgren et al. 2007) and on-site physical experiments (Saiang 2010). In terms of numerical simulation, Li et al. (Li et al. 2018) researched the effect of cavities on crack propagation during blasting loading, while M.J. Nasehi and A. Mortazavi (Nasehi and Mortazavi 2013) studied the effects of the initial stress state and intact rock strength parameters on hydraulic fracturing. This research suggests a strong correlation between the failure mode of rock and its mechanical properties as well as the existence of cavities. Nevertheless, these studies mainly focused on intact rock and did not consider the impact of cracks formed during construction or naturally occurring cracks on rock mass failure. However, compared with cracks, faults pose a greater risk of instability and damage in open-pit mines (Suorineni et al. 1999). The angle between the faults and the stope plays a pivotal role in influencing mining process stability. Bruneau et al. (Bruneau et al. 2003) recorded examples of shaft damage resulting from faults. Through analysis of the rock failure process, Jia and Tang (Jia and Tang 2008) underscored the significant influence of crack angles on the failure mechanisms of tunnels within fractured rock masses. Huang et al. (Huang et al. 2013) found that the presence of weak interlayers reduces tunnel stability leads to uneven stress distribution, and exacerbates tunnel damage. Therefore, fault angles, fracture angles, and weak interlayers play important roles in the stability of engineering structures and

Excavating tunnels in complex geological environments is a challenging task. Tunnel excavations typically encounter need to be fully considered in engineering design to ensure stability and safety.

The aforementioned studies primarily focused on assessing the stability of tunnels or cavities under quasi-static or static conditions. However, in addition to static factors, dynamic disturbances are also crucial factors that induce rock failure, and their impact can be even more severe (Zhu et al. 2007). Tao et al. (Tao et al. 2020) studied the spalling failure mechanism of rock specimens with elliptical holes under impact loading. Yao et al. (Yao and Xia 2019) conducted dynamic tests using notched semicircular bending specimens and a split-Hopkinson pressure bar (SHPB) apparatus, and revealed that the dynamic fracture toughness of rocks decreases with increasing preloading. Kaiser et al. conducted numerical simulations on potential rockburst events following tunnel excavation and established numerical techniques that can effectively predict fracturing around tunnels (Cai and Kaiser 2005; Cai et al. 2004), and support techniques that can enhance production safety (Gao et al. 2019; Kaiser and Cai 2012). Weng et al. (Weng et al. 2017) revealed the fracture behaviour of microtunnel rock specimens under uniaxial compression and impact loads. Subsequently, Weng et al. (Weng et al. 2018) demonstrated that the impact orientation has a significant impact on the failure mode of rock cavities. Feng et al. (Feng et al. 2019) investigated the effects of crack inclination, position, friction coefficient, and lateral pressure coefficient on rock failure when cracks exist around a tunnel under unloading. Research has illustrated that in more severe rock failure situations, a mutually connected network of cracks can lead to more extensive damage to the tunnel.

Researchers have also conducted a series of studies on the practical aspects of tunnel excavation. For example, Li et al. (Li et al. 2024a) studied the effects of intact surrounding rock, open fissures, and filled fissures on tunnel excavation, obtaining different damage patterns of tunnels and fissures under various conditions. Zhao et al. (Zhao et al. 2020b) investigated the dynamic failure behavior of tunnel surrounding rock using the general particle dynamics (GPD) technique, predicting parameters, such as the ejection velocity of the tunnel rock mass, rockburst, and scattered rocks. Li et al. (Li et al. 2024b) studied the destruction behavior of tunnel structures and surrounding rock under different stress states using numerical simulation methods, acoustic emission technology, and digital image correlation (DIC) technology, and found that the inclination angle of the horizontal centerline of boreholes has a significant impact on rock strength, showing a trend of increasing first and then decreasing. Chen et al. (Chen et al. 2019) conducted uniaxial compression tests on granite specimens with bilateral

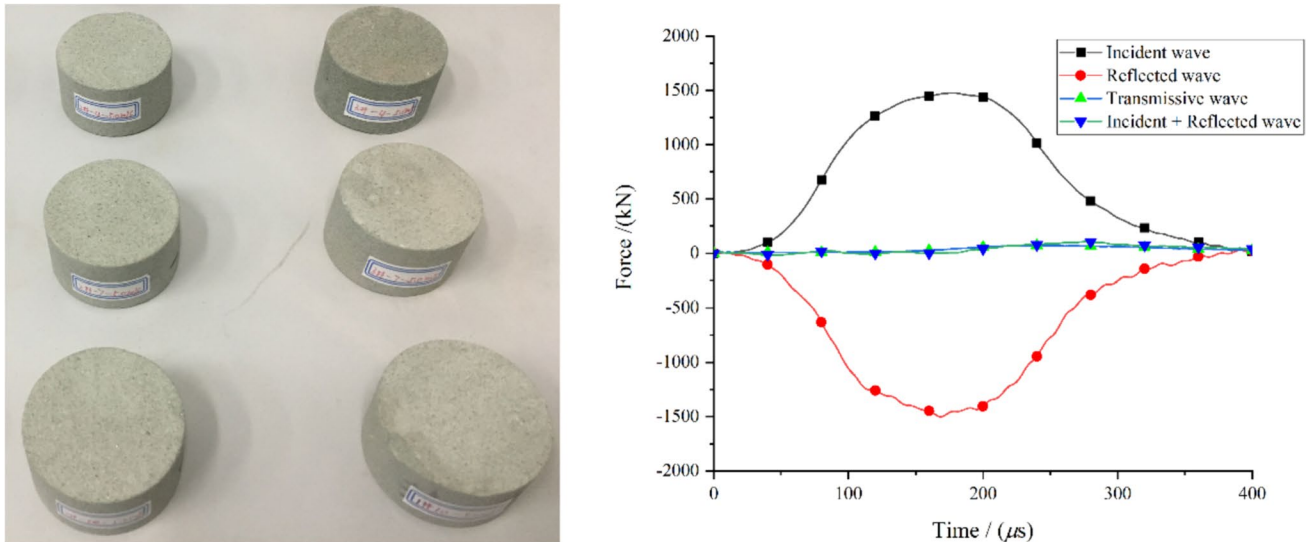


Fig. 1 Dynamic tensile strength of sandstone specimens subjected to SHPB tests

defects, revealing that the crack angle has a significant influence on the crack strength, crack process, and stress distribution, while minor variations in the tunnel opening shape have a smaller impact on the crack strength, crack process, and stress distribution. Zhao et al. (Zhao et al. 2020a) conducted compression tests on actual rock samples with trapezoidal openings under different in-situ stress conditions, obtaining the evolution laws of the strain distribution near the opening, crack propagation, fracture patterns, and rock bursts under different in-situ stresses. The aforementioned studies mainly focused on static fracture, with relatively few studies on the stress distribution patterns of rock surrounding tunnels and fracture modes under dynamic loads.

At present, tunnel engineering analysis mainly focuses on basic mechanical characteristics, which are highly important for understanding rock engineering. Nevertheless, in practical engineering, more emphasis is placed on the failure modes and stress distribution patterns of tunnels. In particular, when there are cracks or other defects near a tunnel, the interaction between an impact stress wave and the tunnel results in a complex stress field around the tunnel. In addition, the direction of the impact stress wave significantly affects the fracture behaviour of the surrounding rock and affects the overall strength of the rock mass. At present, our understanding of these engineering issues remains insufficient. When there are cracks exist around a tunnel, they may alter the stress distribution around the tunnel when subjected to impact stress waves. This is crucial for the design of support systems for tunnel failures. Therefore, to compensate for this deficiency, based on stress wave and fracture mechanics theories, this study established a tunnel model with external cracks for physical experiments and investigated the fracture characteristics of the model and the variation in the stress

field and failure modes near the tunnel under the interaction of the tunnel and cracks. The research results provide insight into engineering applications and perspectives for the design and support of underground tunneling projects.

2 Determination of Mechanical Parameters

2.1 Dynamic Physical Parameters Measured

Dynamic physical parameters are pivotal in investigating the mechanical behaviour of materials under dynamic conditions. In this experiment, the dynamic tensile strength was calculated using a Brazilian disc (BD) test, impacted by an SHPB apparatus, as displayed in Fig. 1. The BD specimens utilized in this experiment had a diameter of 50 mm and a thickness of 25 mm. A total of six BD specimens were measured, and the resulting test data are presented in Table 1. These physical parameters, derived from the experimental data, were incorporated into subsequent numerical simulations.

2.2 Elastic Properties of the Investigated Sandstone

Prior to the impact test, a Sonic Viewer-SX instrument was used to measure the longitudinal wave velocity (C_d) and shear wave velocity (C_s) of the selected material. Subsequently, the Rayleigh wave velocity (C_R), dynamic elastic modulus (E), and Poisson's ratio (ν) were calculated using the following formulas. The investigation involved six cylindrical sandstone samples with a diameter of 50 mm and a length of 100 mm. The test results for the six cylindrical samples are shown in Table 1. These physical parameters

Table 1 Basic physical and mechanical properties of the studied green sandstones

Material	Density/(g/cm ³)	Elastic modulus/ (GPa)	Poisson's ratio/ ν	Tensile strength/ (MPa)	Longitudinal wave velocity/(m/s)	Shear wave velocity/ (m/s)
Green sandstone	2.265	13.57	0.171	23~25	2549.4	1459.2
LY12CZ	2.35	71.70	0.300			

obtained from the experiment were utilized in subsequent numerical simulations. The calculations for the Rayleigh wave velocity (C_R), dynamic elastic modulus (E), and Poisson's ratio (ν) are as follows (Zhang et al. 2021):

$$\begin{cases} C_d = \sqrt{\frac{E(1-\nu)}{(1+\nu)(1-2\nu)\rho}} \\ C_s = \sqrt{\frac{E}{2\rho(1+\nu)}} \end{cases} \quad (1)$$

$$\left(2 - \frac{C_R^2}{C_s^2}\right)^2 = 4\sqrt{\left(1 - \frac{C_R^2}{C_d^2}\right)\left(1 - \frac{C_R^2}{C_s^2}\right)}. \quad (2)$$

3 Impact Test Design

3.1 Experimental Model

Green sandstone, widely utilized for investigating the mechanical attributes of rock under dynamic loads, constituted the experimental specimens due to its excellent homogeneity in our study. For the experimental model, an “outside crack around a tunnel” (OCT) configuration was utilized which can provide a long enough crack propagation distance for the whole dynamic crack propagation process. The rock plate used in the model had dimensions of 325 mm × 250 mm × 30 mm, including a tunnel-shaped cavity measuring 50 mm × 50 mm × 30 mm (see Fig. 2) which was based on large single cleavage semi-circle compression (Ying et al. 2019). To meet practical requirements, a minimum crack width of 1 mm was set. The purpose of this study was to investigate the dynamic fracture behaviour and distribution evolution of a cracked tunnel model under dynamic effects.

3.2 Model Test

In the model test, green sandstone was selected as the raw material for testing. This type of sandstone has a uniform texture and abundant availability. Analysis using an X-ray

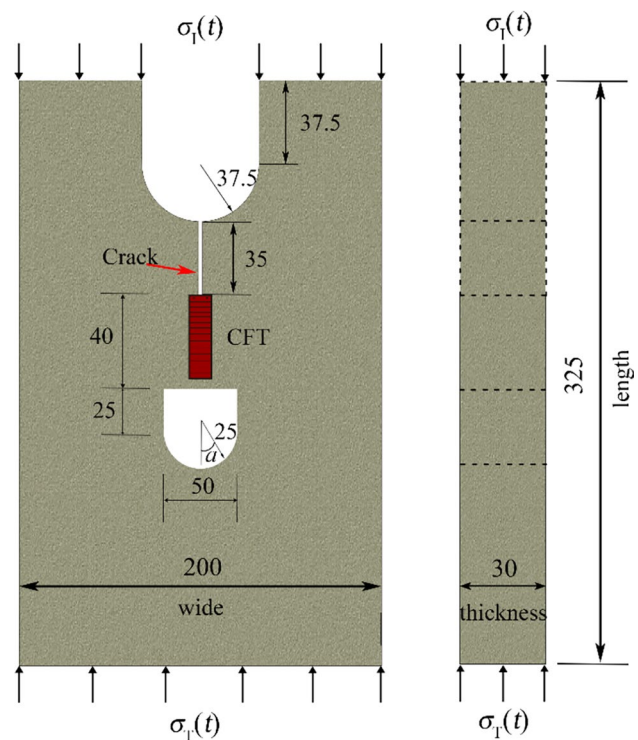


Fig. 2 Illustration of the impact model

diffractometer confirmed that the sandstone primarily consists of three mineral components: muscovite, analcime, and quartz. The size distributions of these minerals are as follows: 0.05 mm–0.2 mm for quartz, 0.08 mm–0.2 mm for analcime, and 0.04 mm–0.08 mm for muscovite (refer to Fig. 3).

Previous studies have shown that green sandstone is an ideal rock type for studying dynamic fracture experiments, obtaining crucial fracture parameters and observing the crack propagation behaviour of fractured rock masses (Ying et al. 2020). The dynamic physical parameters of the green sandstone specimens were measured according to the relevant standards established by the International Society of Rock Mechanics (ISRM) (Aydin 2009), as presented in Table 1. To conduct the dynamic experiments, a drop weight impact test device was employed to investigate the dynamic fracture behavior of the OCT model from various orientations. The data acquisition system consisted of

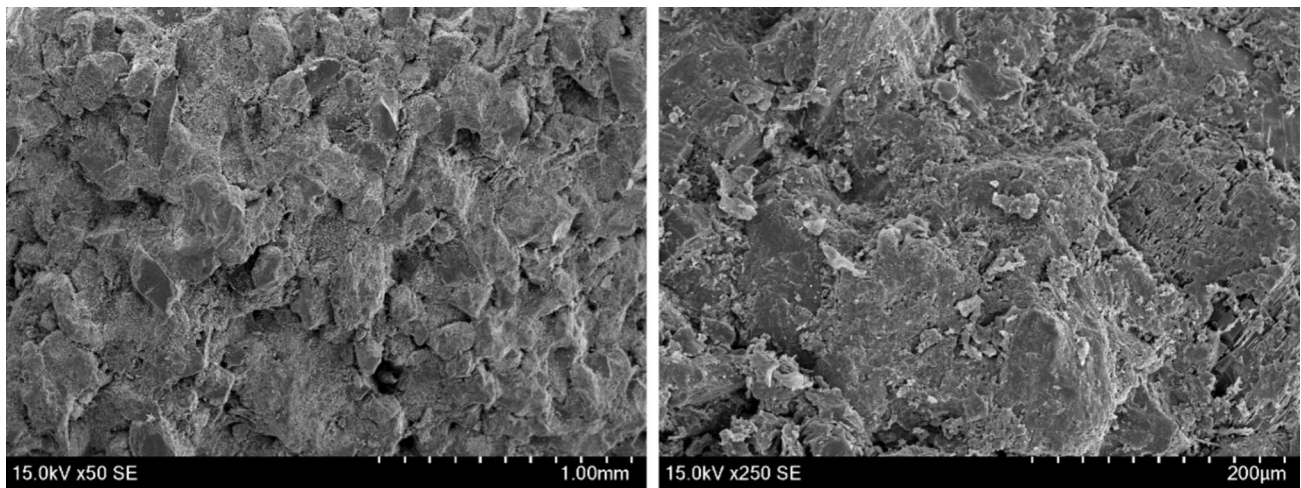


Fig. 3 Microstructures of green sandstone

an impact hammer, incident bar, transmission bar, sensor, and data acquisition equipment. The incident bar measured 300 mm × 3000 mm × 40 mm, while the transmission bar measured 300 mm × 2000 mm × 40 mm, both of which were made of aluminium alloy. A strain gauge was installed between the incident and transmission bars to record the stress wave effect during the dynamic impact process. The loading hammer had a loading range of 0–10 m, and the impact velocity was measured using an infrared velocimeter (refer to Fig. 4a).

Scholars have focused on crack propagation behaviour and crack initiation time (CIT) as fundamental fracture mechanics parameters for studying the dynamic fracture behaviour of rock. To measure the crack fracture time and calculate the crack extension velocity and fracture toughness, a crack fracture tester (CFT) was utilized. The CFT consisted of 21 parallel-connected filaments with a pitch of 2 mm, resulting in a total length of 42 mm. The principle of the CFT is depicted in Fig. 4b. In the connection circuit, two protective resistors with resistance values of 51 Ω were connected in series with the CFT and in parallel with each other. This test method is extensively employed for observing macroscopic crack rates.

3.3 Model Test Results

Strain gauges applied to the incident and transmission bars were used to acquire the signal data. The recorded strain–time–history curve is illustrated in Fig. 5 (a). After conducting several repetitions of the experiments, it was determined that the impact height should be set to 2.8 m. The peak value observed in the stress–time curve is approximately 35 MPa. This dynamic loading can be calculated using the following formula:

$$\begin{aligned}\sigma_i &= E_i(\varepsilon_i(t) + \varepsilon_r(t)) \\ \sigma_t &= E_t\varepsilon_t(t),\end{aligned}\quad (3)$$

where $\varepsilon_i(t)$, $\varepsilon_r(t)$, and $\varepsilon_t(t)$ represent the strain gauge signals received from the incident, reflected, and transmitted strain signals, respectively, and E_i , E_t represent the elastic moduli of the two bars.

The CFT monitoring voltage signal provides valuable information about the crack ignition time, fracture moment, and crack arrest time of the impact model. Figure 5 (b) illustrates these parameters. Assuming that the time for the stress wave to reach the top of the specimen is 0 µs, it is observed that the CIT of the specimen at -60° is 190.4 µs. Additionally, the average crack growth speed is 503.7 m/s, with a maximum growth rate of 896.23 m/s and a minimum of 36.39 m/s.

Throughout the crack growth process, there is a distinct period of slower growth, indicating a temporary halt in crack propagation (Foster et al. 2011). Analysing the overall fracture results, it is evident that the crack grows faster during the crack initiation stage (stage 1, depicted in grey), followed by a gradual decrease in speed during the expansion process. At a certain point, stagnation can be observed, which corresponds to the crack arrest stage (stage 2). Due to the superposition effect of the stress wave, the crack underwent another rapid growth stage (stage 3, shown in yellow).

In summary, the CFT monitoring voltage signal allows for the determination of crucial crack behaviour properties, such as the CIT, fracture moment, and crack arrest time. The crack growth process exhibits distinct stages, including initiation, expansion, and potential arrest, all of which are influenced by the complex interaction of stress waves.

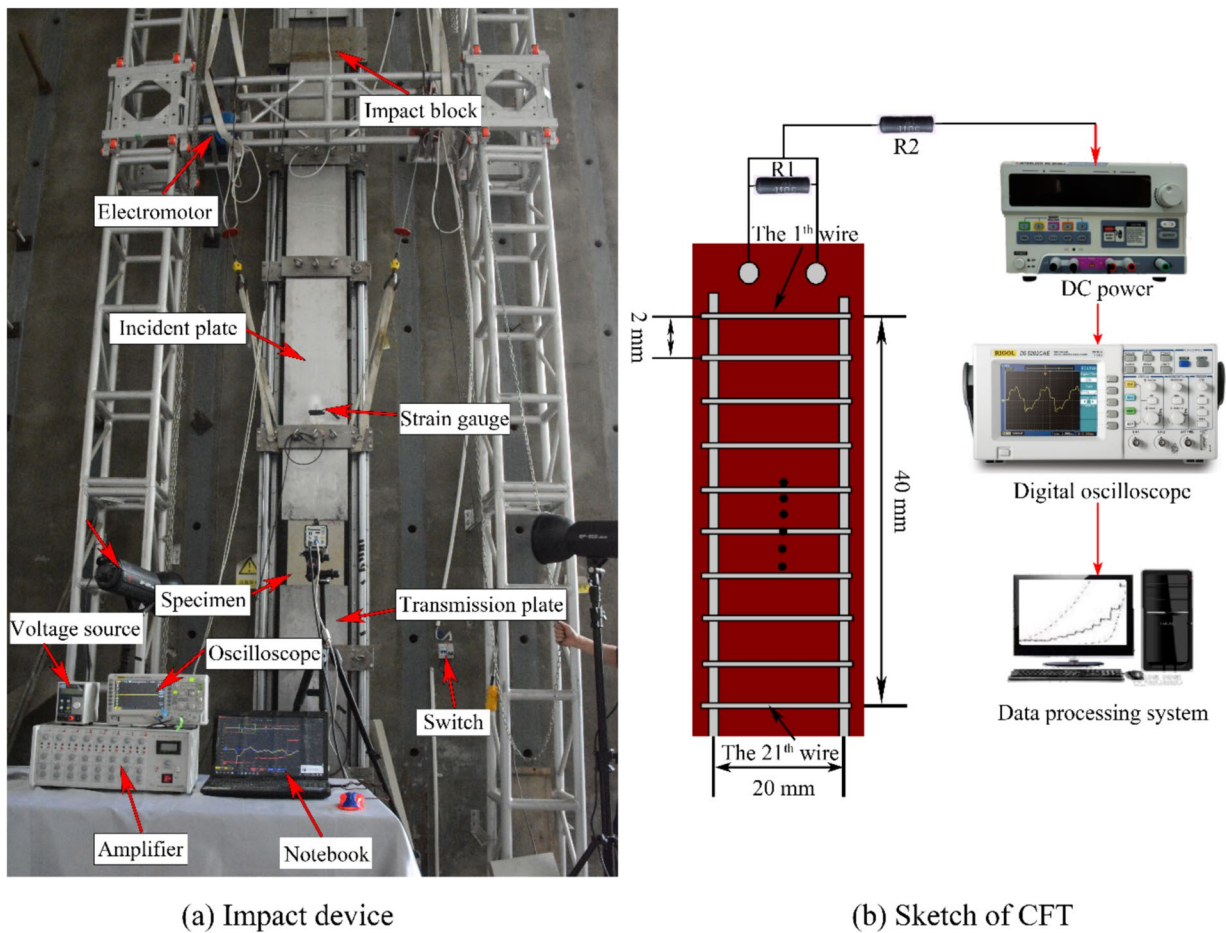


Fig. 4 Physical experimental system and CFT measuring system

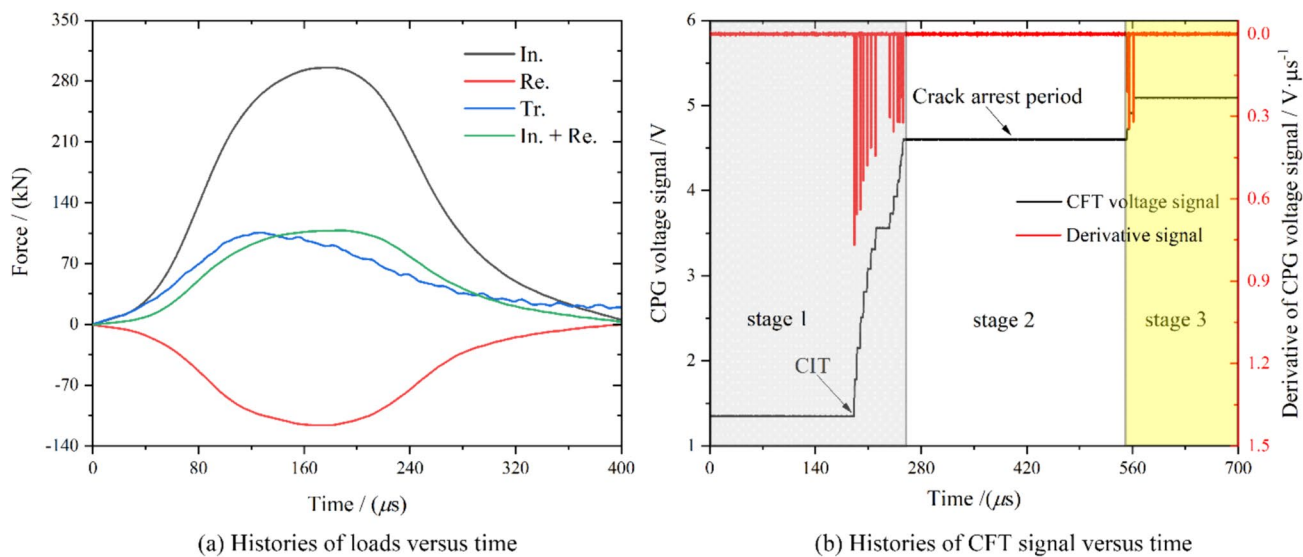


Fig. 5 Strain–time history and CFT test results

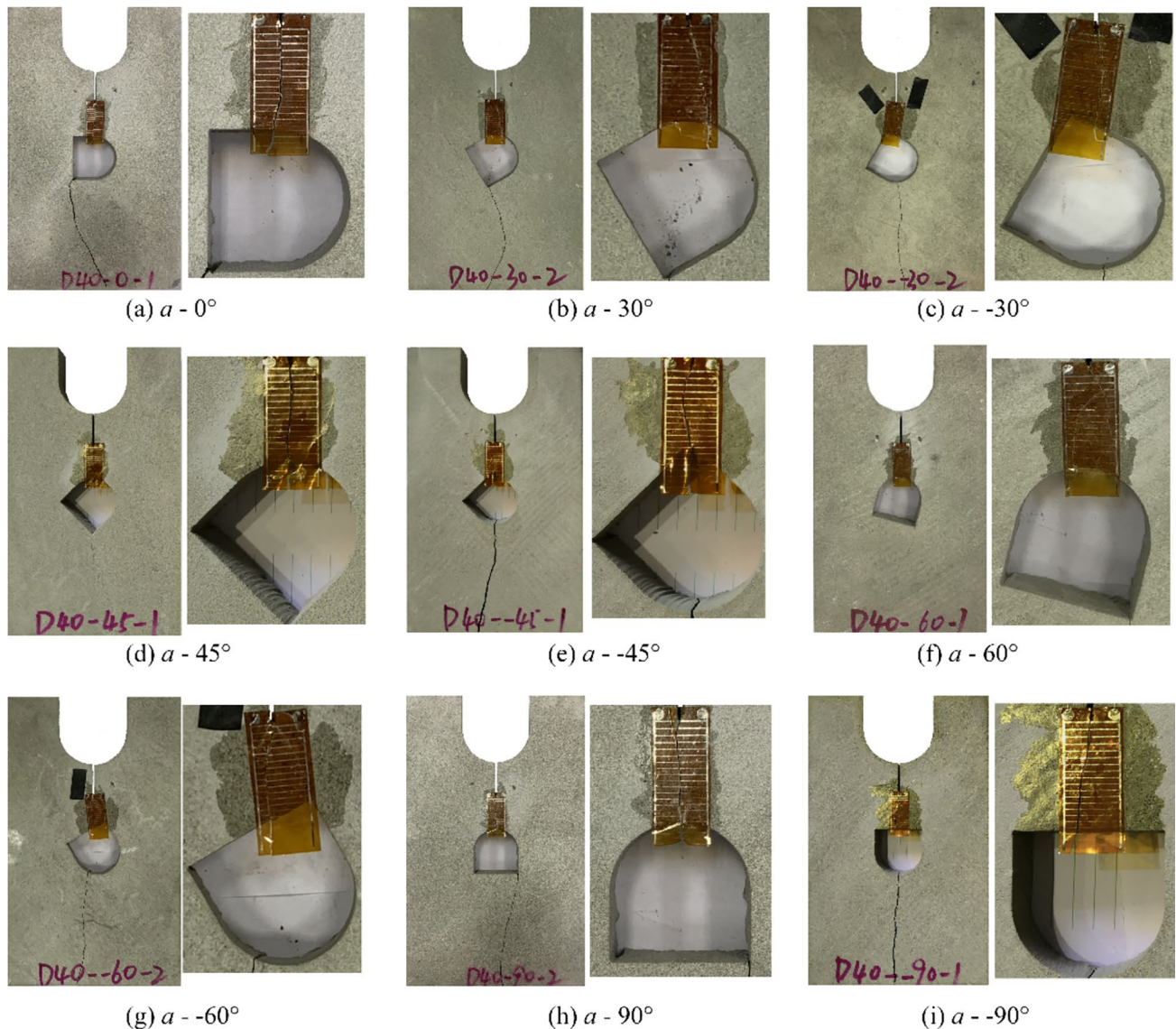


Fig. 6 Model test results for different impact directions

3.4 Crack Path Results

Figure 6 presents the results obtained from different impact directions, and the second figure provides an enlarged view of the crack propagation path. From the figure, it is evident that the crack propagation path does not follow a straight line but rather follows a curve. The one-dimensional wave generated by the impact system moves parallel to the prefabricated crack, indicating that the shock wave and the prefabricated crack propagate in parallel. Far from the tunnel, the crack could be considered a mode I crack, with a nearly linear extension (Liu et al. 2020).

During the experiments, the prefabricated cracks all propagated, but their paths varied depending on the incident angle, causing deflection during crack propagation.

This shows that the presence of a tunnel affects crack propagation and that this effect is influenced by the direction of the impact load. For example, when the incident angle is 0° , the shock wave propagates perpendicular to the tunnel wall, and the prefabricated crack propagates towards the spandrel. At angles of -45° and -60° , the prefabricated crack deflects towards the corner of the tunnel. When the angle is -90° , the shock wave spreads perpendicular to the tunnel floor, and the prefabricated crack propagates towards the middle of the floor. At an angle of -30° , the prefabricated crack extends a certain distance from the corner of the tunnel.

For angles of 0° , 45° , and 90° , the prefabricated crack eventually propagates past the tunnel along the same orientation as the prefabricated crack. This implies that the

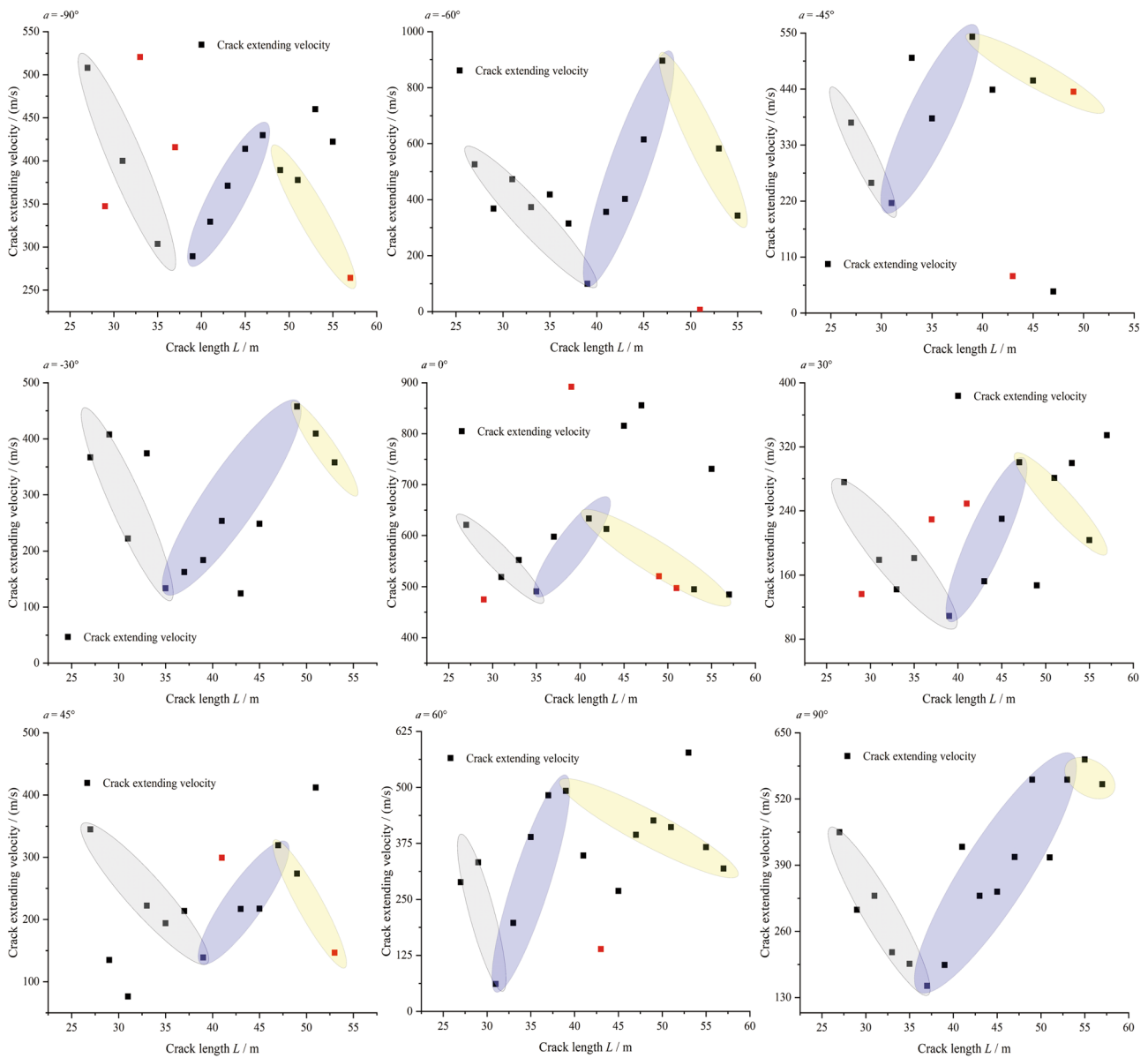


Fig. 7 Experimental results of the crack growth velocity under the different impact directions

impact load direction has a limited effect on the damage mode in these instances. However, at angles of 30° and 60° , the crack propagation path mainly tilts towards the vault, and the degree of this tilt may also be influenced by the material’s homogeneity. These observations are primarily attributed to the interaction between the incident and reflected stress waves during crack propagation around the tunnel.

3.5 Crack Initiation Time and Crack Extension Velocity

This section describes the determination of the crack extension velocity in the context of CFT. The velocity was computed based on the time difference between the fracturing of two tension wires and the distance between them. This section also discusses crack propagation under dynamic loading from different angles.

According to Fig. 7, the crack propagation velocity initially undergoes a high-speed stage characterized by rapid crack initiation. Subsequently, crack propagation decelerates, possibly leading to crack arrest (as depicted by the grey part of Fig. 7).

Table 2 Prefabricated crack propagation data

α ($^{\circ}$)	- 90	- 60	- 45	- 30	0	30	45	60	90
Average crack extension velocity/(m/s)	445.9	503.7	418.3	340.7	699.5	265.4	300.3	392.5	429.8
CIT/(μ s)	226.6	190.4	398.6	283.2	311.9	355.9	212.8	342.5	275.6

However, due to the superimposed effects of reflected waves and incident waves, the cracks may extend again, as shown in the blue part of Fig. 7. As energy dissipates, the crack propagation velocity shows a downwards trend once more in the yellow part, indicating a potential crack arrest phase similar to the earlier deceleration phase. The dispersion of some experimental data points may arise from test errors and other factors.

Furthermore, Freund (Freund 1990) suggested that the crack extension speed should not surpass the Rayleigh wave speed, which is lower than the shear wave speed (Viktorov 1967). Consequently, crack propagation lags behind stress wave propagation. Several experimental studies, including those conducted by Liu et al. and Wang et al. (Liu et al. 2020; Wang et al. 2017), reported that the reported crack propagation velocity in sandstone under impact loading is approximately several hundred meter meters/second. Zhang and Zhao (Zhang and Zhao 2014) also reported crack propagation velocities ranging from 300 to 650 m/s in sandstone. For example, Li et al. (Li et al. 2018) observed an average crack extension velocity of 529.3 m/s in sandstone subjected to dynamic loading.

In the experiment, the longitudinal wave velocity of the sandstone was approximately 2550 m/s. The delay time for stress waves to propagate to the crack tip and initiate crack formation was assumed to be equal to the delay time for the shock wave to reach the tunnel face and cause a new crack to form. The time taken for longitudinal wave propagation to a distance of 40 mm (the length of the CFT) was 15.69 μ s. The average crack velocity was conservatively 300 m/s. When the distance for prefabricated crack extension was 4.71 mm, the obtained crack extension velocity did not consider the potential influence of new cracks forming in the tunnel. Therefore, the fracture time of the first 2–3 tension wires in the CFT was credible, indicating that these wires fractured successively due to the extension of the prefabricated crack. The fracture of tension wires beyond the first 3 wires may have been influenced by the formation of new cracks in the tunnel. Hence, it was possible to observe crack extension velocities exceeding the range of 300–650 m/s in some tests or in cases where there were less data available for measuring the crack extension velocities, such as for inclination angles of -60° and $\pm 45^{\circ}$. Therefore, the experimental results are reliable. In the experiment, the average crack extension velocity was obtained by comparing the time difference between the first and last tension wire fractures and the

corresponding extension distance. The fracture time of the first tension wire in the fracture test specimen represents the CIT. The CIT and the average crack extension velocity are shown in Table 2.

It was observed that crack extension velocities exceeding the range of 300–650 m/s were possible in the experiments. Additionally, limited data are available for measuring crack extension velocities, particularly for inclination angles of -60° and $\pm 45^{\circ}$. Despite these factors, the experimental results were deemed reliable. To determine the average crack extension velocity, the researchers compared the time difference between the fracturing of the first and last tension wires with the corresponding extension distance. The fracture time of the first tension wire in the fracture test specimen represented the crack initiation time. These CITs and the average crack extension velocities are shown in Table 2 of the research report or publication.

The CITs for different impact directions exhibit a significant difference without any discernible pattern. The likely cause of this disparity was the application of grease on the incident and transmitting ends of the specimens for the experiment, to reduce frictional forces. Grease acts as a cushion, and variations in its thickness during application may lead to different levels of buffering in the propagation of stress waves, resulting in irregularities in CIT. To further analyse the CITs, numerical simulations were performed, as discussed in subsequent sections.

The majority of the average crack extension velocities fall within the range of 300–650 m/s, except for cases where the angle α is 0° or 45° . This finding aligns with the previous studies on crack propagation velocity in sandstones, specifically the research conducted by Zhang and Zhao (Zhang and Zhao 2014). The discrepancy in crack extension velocity measurements in the test data could be attributed to two factors. First, there may have been simultaneous initiation and extension of prefabricated cracks and tunnel cracks, resulting in fractures occurring within the same timeframe. Second, variations in the closest distance between the prefabricated cracks and the tunnel could arise from fabrication errors in the experimental model as well as the rotation of the tunnel model. Since the high-speed imaging system was not utilized during the experiment for additional observations, further explanations and insights were obtained through subsequent numerical simulations.

Table 3 Mechanical properties of the sandstone

Material	P(kg/m ³)	σ_t (MPa)	K (GPa)	G (GPa)	E_d (GPa)	ν	C_d (m/s)	C_s (m/s)	C_R (m/s)
Sandstone	2265	24.842	6.741	5.826	13.57	0.171	2563	1607.4	1457.6

4 Numerical Simulations via the Finite Difference Method (FDM)

Numerical simulations were conducted using the FDM to analyse the crack extension behaviour and failure modes of tunnel structures under impact loads. A model of the tunnel structure and surrounding rock materials was established, as depicted in Fig. 2. The average pore size of the model was set to 1 mm. To ensure accurate calculation results and prevent significant deformation of the overall mesh during the simulation, the FDM provided by AUTODYN was utilized. This method effectively avoids noticeable deformation of the rock material throughout the computational process, ensuring computational efficiency and the reliability of the calculations.

The FDM has been utilized in the previous studies (Areias et al. 2016; Nasehi and Mortazavi 2013; Wong and Li 2013), and its effectiveness in accurately capturing the behaviour of rock materials during dynamic events has been demonstrated. By employing this method, the simulations in this study aim to provide reliable insights into the crack propagation behaviour and failure modes of tunnel structures under impact loads.

4.1 Failure Criterion of Sandstone

In our previous study (Zhu et al. 2007), we discussed the constitutive equations and advantages of using the AUTODYN software for dynamic problem-solving in detail. In such dynamic tests, the pressure or deformation experienced by the sandstone has minimal significance and a negligible effect on thermodynamic entropy. Therefore, we attributed the pressure or deformation solely to the volume and density of the sandstone. To describe the failure behaviour of sandstone, we utilized a linear equation of state (EOS). The linear EOS can be represented by the following equation:

$$P = \kappa \mu = \kappa \left(\frac{\rho}{\rho_0} - 1 \right), \quad (4)$$

where P represents the pressure of the sandstone, κ denotes the bulk modulus, and ρ and ρ_0 are the actual density and reference density of the rock, respectively.

To comprehend the failure patterns in the cracked tunnel model subjected to impact loading, we analysed the major principal stress. Failure occurs in an element when the principal tensile or shear stress exceeds the dynamic tensile or shear strength of the sandstone. The major principal stress criterion is expressed as.

$$\sigma_1 > [\sigma] \text{ or } t_{12} > [t_r], \quad (5)$$

where σ_1 represents the principal tensile stress, $[\sigma]$ signifies the dynamic tensile strength of the rock, t_{12} indicates the principal shear stress, and $[t_r]$ manifests the dynamic shear strength of the rock.

In recent years, extensive research has been conducted on the meshing of grid elements, leading to significant advancements (Areias et al. 2016, 2013; Areias and Rabczuk 2017). In our study, triangular unstructured grid elements which minimally affect crack behavior, were used in the AUTODYN software (Li and Wong 2012). The tunnel model consisted of 76,710 elements, with a finer grid near the crack tip, as shown in Fig. 9. To replicate the loading conditions of the impact experiment in Fig. 4, we applied a curve crest of 178.69 kN on the incident bar. The bottom of the concrete cushioning served as a nonreflecting boundary.

The initial crack in the model had dimensions of 35 mm in length and 1.0 mm in width. The material parameters employed in the numerical model can be found in Table 3. These parameters were determined using the standard tests in accordance with the ISRM recommendations. The tests involved measuring the longitudinal wave velocity (C_d), shear wave velocity (C_s), and dynamic tensile strength (σ_t) of the material. As a result, uncertainty analysis to assess the influence of the input parameters was deemed unnecessary for this particular study (Hamdia et al. 2017; Vu-Bac et al. 2016).

4.2 Crack Initiation Time

Numerical simulations were conducted to calculate and analyse the CIT, as shown in Fig. 8, as the experimental results revealed irregular patterns due to the influence of the grease on the tested cracks. The CIT results of the tunnel corners are very similar, which shows the reliability of the test, and the overall trend is a “W” shape with increasing incident angle. When the incident angle is $\pm 45^\circ$, the crack CIT is the shortest which means that the surrounding rock is most prone to failure; compared with positive incident angles, negative incident angles correspond to situations in which cracks are more difficult to initiate.

4.3 Crack Dynamic Initiation Toughness

For rock fracture studies, it is important to evaluate the stability of a crack under external loads by considering not only the crack critical initiation toughness (CDIT), propagation speed, and other parameters but also the crack dynamic initiation

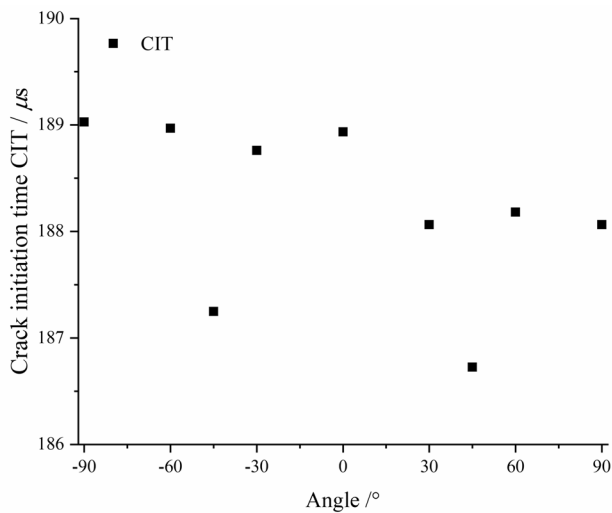


Fig. 8 CIT under the different impact directions

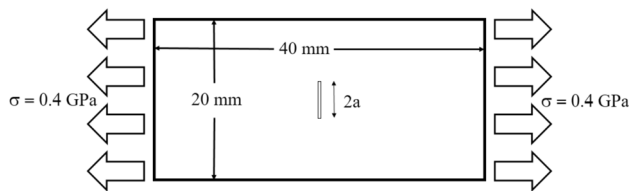


Fig. 9 Central cracked plate model schematic

toughness (DIT). The DIT quantifies the material resistance to dynamic cracks during initiation and propagation. In this study, we utilized the displacement extrapolation method to calculate the stress intensity factor (SIF) at the crack tip. The DIT was subsequently derived from the CIT. The calculation formulas can be expressed as follows:

$$K_{li}(t) = \frac{E v_i(t)}{(k+1)(1+\nu)} \sqrt{\frac{2\pi}{r_i}} \quad (6)$$

$$\kappa_i(t) = \frac{K_{li}(t)}{\sigma_0 \sqrt{\pi a}},$$

where $K_{li}(t)$ and $\kappa_i(t)$ are the SIFs before and after normalization, respectively; $v_i(t)$ is the crack opening displacement; E represents the elastic modulus; ν is the material Poisson's ratio; and r_i represents the distance from the monitored point to the crack tip.

This project focuses on calculating the dynamic fracture characteristics of cracks using an experimental–numerical approach. To verify the feasibility of the FDM software, a verification process was carried out. Based on published literature (Chen 1975), the model, as depicted in Fig. 9, consists of a cracked plate with a width of 20 mm and a length of 40 mm, with a central crack of $2a = 4.8$ mm. The material

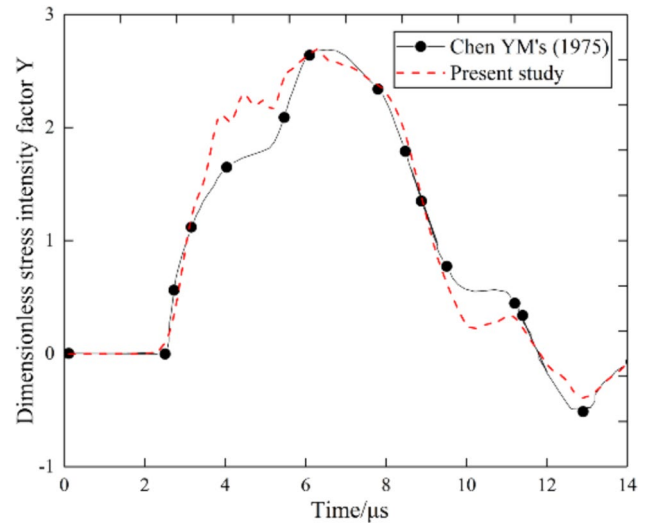


Fig. 10 The numerical results are compared with those of the Chen problem

used in the model is assumed to be a linear elastic homogeneous material with a density of 5000 kg/m^3 , an elastic modulus of 200 GPa, and a Poisson's ratio of 0.3. Additionally, a constant pressure of $\sigma = 0.4 \text{ GPa}$ is applied at both ends of the model.

Moreover, to verify the reliability of the grid, a grid size of 1 mm was calculated and normalized for comparison with the Chen problem (Chen 1975), as illustrated in Fig. 10. The size result was very close to the result of the Chen problem. To improve the efficiency of subsequent model calculations, this project used a grid size of 1 mm for simulation.

4.4 Dynamic Stress Distribution of the Tunnel Model with or Without Cracks

With changes in the tunnel rotation angle, the stress distribution pattern of the tunnel model under the same stress wave can vary significantly. Figure 11 illustrates the temporal distribution of the von Mises dynamic stress when the incident angle $\alpha = -60^\circ$, comparing the cases with and without cracks on the tunnel surface. Initially, the overall structural distribution pattern remains unchanged, as shown by the result at $35.5 \mu\text{s}$. However, as the stress wave propagates, the region between the crack and the tunnel experiences significant disturbances. At $t = 215.9 \mu\text{s}$, when a crack is present, the stress within rock bridges can be twice as high (or even higher) as that in the case without a crack. Conversely, the stress distribution pattern around the tunnel remains relatively consistent. When the crack propagates through the tunnel ($t = 432.2 \mu\text{s}$), the stress distribution pattern near the tunnel changes. The stress concentration area shifts downwards for the tunnel bottom, but the stress magnitude in the absence of a crack is greater than that when a

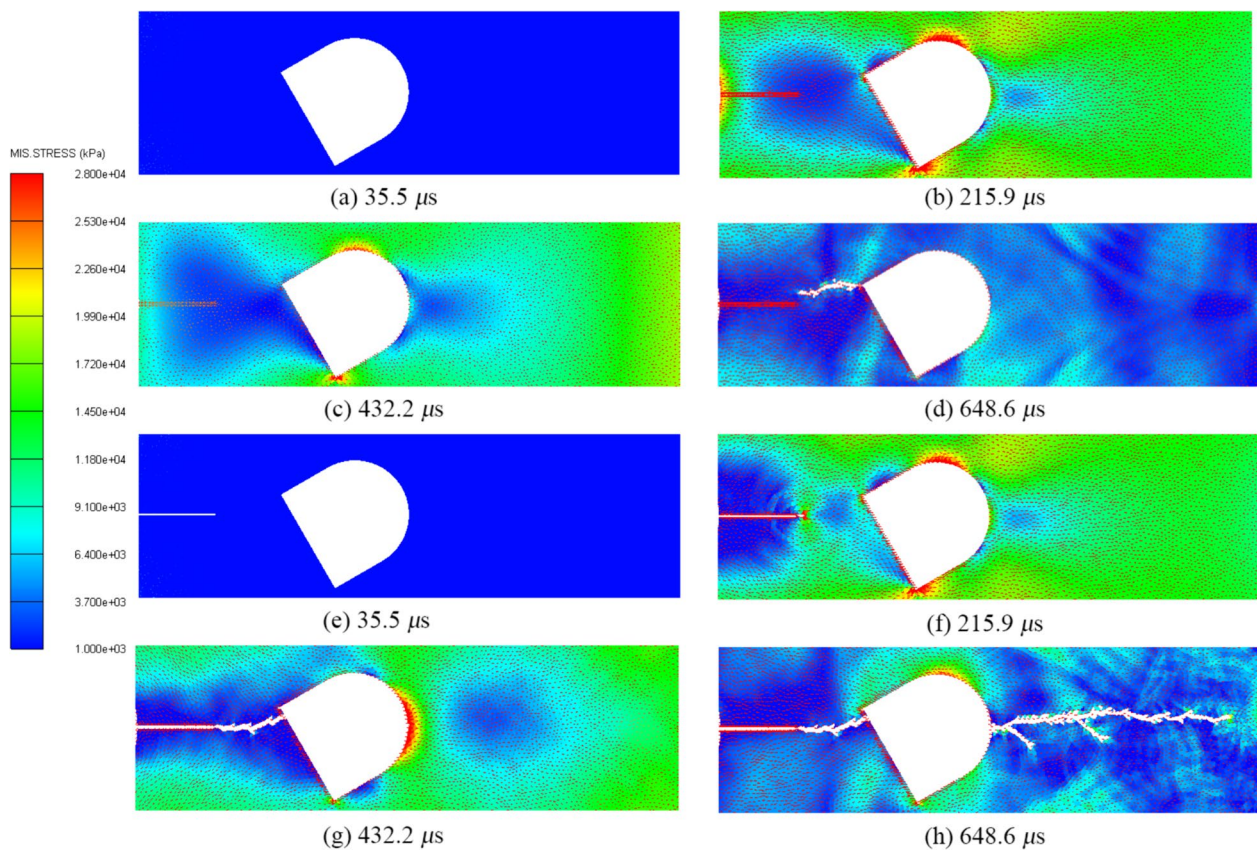


Fig. 11 Time-history distribution of the von Mises stress in the structure under a dynamic disturbance: (a–d): no crack at the tunnel side; (e–h): crack at the tunnel side

crack occurs. However, for the arch region of the tunnel, the major stress concentrations occur on the incident side for structures without a crack, but for structures with a crack, the region of higher stress appears on the transmitted side.

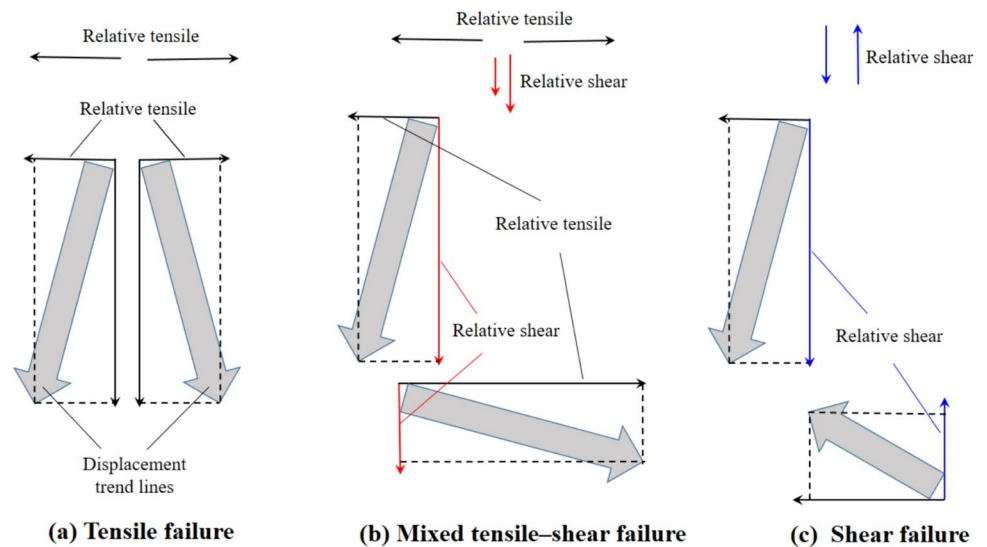
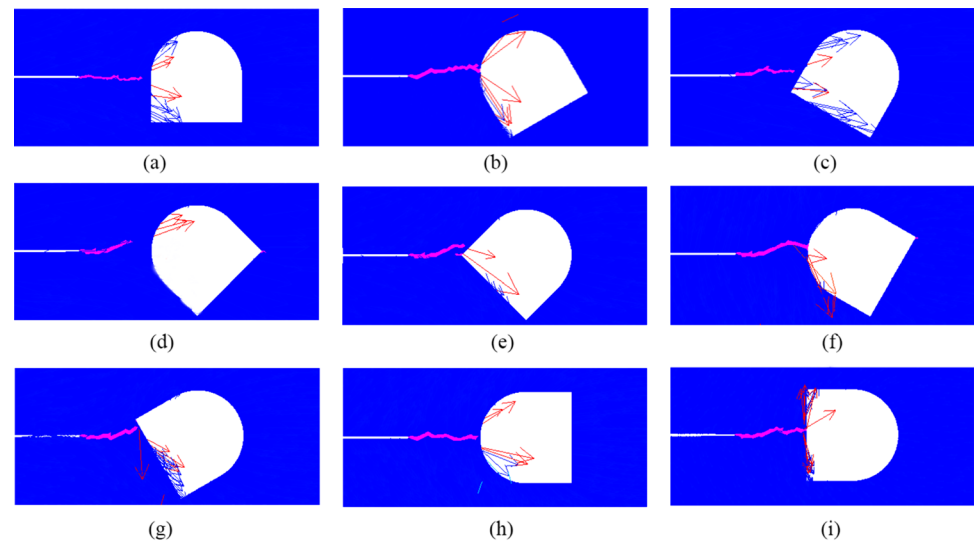
As the stress wave propagates, a new crack forms. For structures without prefabricated cracks, a new crack arises at the corner of the tunnel sidewall, closer to the incident end. However, a new crack appears near the arch crown in structures with the existing cracks, as shown in Fig. 9 (d, h). Additionally, significant differences in the crack propagation length are noted for the same duration. Structures with cracks exhibit longer crack propagation lengths, indicating a greater level of structural vulnerability. Hence, in tunnel engineering, it is crucial to consider not only cracks at the tunnel edge but also cracks farther away, which are highly relevant in tunnel design and maintenance and should be considered to ensure structural safety and reliability.

4.5 Failure Model

Section 3.4 reveals that when a shock wave encounters a preexisting crack, the initial crack propagation is primarily in mode I. However, upon reaching the tunnel working face

and undergoing reflection, the stress field becomes complex, leading to a deviation in the crack propagation pattern and a change in the crack failure mode. Determining whether the crack failure mode corresponds to tensile or shear failure becomes challenging, as the numerical model cannot differentiate between tensile and compressive damage. To address this challenge, the displacement trend line (DTL) method, developed by Zhang (Zhang and Wong 2014), was employed to determine the failure mode. This method categorizes crack morphology into three types: tensile failure, tensile–shear mixed failure, and shear failure, as illustrated in Fig. 12. Tensile failure in rock (Fig. 12a) is characterized by the separation of displacement trajectories, indicating relative tensile displacement. Shear failure in rock (Fig. 12c) is identified by the convergence of DTLs, signifying significant shear effects. DTLs may also exhibit relative tensile–shear characteristics, indicating mixed tensile–shear failure (Fig. 12b).

The failure modes of the rock surrounding the tunnel were analysed numerically, and the results are presented in Fig. 13. Initially, during the early stages of crack propagation, the crack extension path appears relatively straight, suggesting that crack initiation and extension are influenced

Fig. 12 DTL diagram. (Zhang and Wong 2014)

Fig. 13 Numerical simulation of the fracture mode at the late crack stage: (a) 0° , (b) 30° (c) -30° , (d) 45° , (e) -45° , (f) 60° , (g) -60° , (h) 90° , and (i) -90°


primarily by the incident stress wave and are only minimally affected by the reflected wave. However, as the crack extends, the impact of the reflected wave gradually becomes more pronounced.

Based on the numerical analysis, it was determined that when the angle of incidence a is 0° , 30° , -30° , or 90° , the crack extension on the tunnel entrance side demonstrates a tensile failure mode. On the other hand, when $a = \pm 45^\circ$, shear failure was observed on the tunnel entrance side, and a similar phenomenon occurred at $a = \pm 60^\circ$. Additionally, during the extension process, at -45° , cracks emerge at the bottom corner of the tunnel, and subsequently merge and penetrate the cracks that propagated from the preexisting crack. This indicates that both the preexisting crack propagation and new crack extension at the bottom corner of the tunnel can occur simultaneously during the impact process. This observation aligns with the experimental data on crack

propagation velocity, where the specimen with $a = -45^\circ$ exhibits slightly slower crack propagation than the others. Moreover, when $a = -90^\circ$, a tensile-shear mixed failure mode is observed in the same region. However, all new cracks originating from the transmission side of the tunnel are qualitatively classified as tensile failure.

4.6 Dynamic Stress Concentration Factor (DSCF)

When stress waves interact with cracks in the rock surrounding a tunnel, various transmission and reflection phenomena occur, leading to the formation of a complex stress field near the tunnel. The presence of a crack in conjunction with a tunnel creates a stress concentration phenomenon that has attracted significant attention from researchers.

To predict the dynamic failure behaviour of fractured rock masses in tunnels, this research focused on analysing the

changes in radial and circumferential stresses near a tunnel. To facilitate the analysis, a local coordinate system was established with the centre of the tunnel as the origin of the coordinate system. The tunnel vault is considered 0° , and rotation is measured in a clockwise direction from 0° to 360° , as depicted in Fig. 15(a). The calculation expressions for the radial and circumferential stresses are derived using the following formula:

$$\sigma_{\theta\theta} = \sigma_x \cos^2 \theta + \sigma_y \sin^2 \theta - 2\tau_{xy} \sin \theta \cos \theta \quad (7)$$

$$\sigma_{rr} = \sigma_x \cos^2 \theta + \sigma_y \sin^2 \theta + 2\tau_{xy} \sin \theta \cos \theta, \quad (8)$$

where $\sigma_{\theta\theta}$ is the radial stress, σ_{rr} is the circumferential stress; and σ_x , σ_y and τ_{xy} are the stress the X directions, the stress in the Y direction and the shear stress of the monitoring points, respectively.

Rock surrounding brittle tunnels, such as the green sandstone mentioned in this study, exhibits fracture behaviour that is strongly influenced by the circumferential tensile stress. To analyze the dynamic fracture patterns in fractured tunnels subjected to dynamic disturbances, the DSCF (Yi et al. 2014) was employed. This factor is defined as the ratio of the circumferential stress to the incident wave amplitude in an equivalent area without the presence of a tunnel. According to the calculation results, a negative DSCF value indicates the concentration of tensile stress. Furthermore, the magnitude of the negative value reflects the severity of tensile stress concentration. In other words, smaller negative values correspond to a greater concentration of tensile stress in the tunnel surrounding rock. To make it easier to distinguish the DSCF around the tunnel after different impact loading directions, the tunnel was divided as shown in Fig. 15(a), and the angle was rotated clockwise to positive to establish a local polar coordinate system for the surrounding rock of the tunnel. To compare the influence of external cracks on the DSCF of the tunnel, a numerical model without cracks was also calculated. To compare the two cases, the kinetic energy and total energy input in the study structure are the same, as shown in Fig. 15(b). Finally, the DSCF results of the rock surrounding the tunnel under the different impact loading directions are obtained, as shown in Fig. 14. Notably, as the crack has already initiated in both the test and numerical outcomes, this implies a substantial concentration of stress at the crack's tip. Consequently, the calculation of the DSCF in the immediate vicinity of the crack is deemed unnecessary.

The figure indicates that the DSCF around the tunnel increases in various positions with different impact loading directions, but the concentration areas are mainly in the tunnel bottom (225° and 135°), vault (0°), and arch arc (45° and 60°), which are very similar to the test results. The results for the crack-free structure (part of the red curve) show that

the predicted danger area is basically the same, but for the structure with cracks, the DSCF is larger; in both cases, the maximum difference is 20 times greater (at 0°), and the average difference at each angle is 6.19 times, which indicates that cracks in this structure have a significant impact on tunnel stability. This is because before the shock wave reaches the working face of the tunnel, the overall tunnel structure should be stable, with no fluctuations in the stress field around the tunnel. After the impact stress wave reaches the tunnel face, the stress field around the tunnel fluctuates due to the transmission and reflection of the stress wave. When there are cracks around the tunnel, the structure will be affected by the crack interface, resulting in this fluctuation. Figure 15(c, d) shows the first principal stress–time–history curve of each monitored point of the tunnel for $a = -60^\circ$. The grey area shows the area that first began to fluctuate. The starting time of the fluctuation is 0.5225 ms when there is no crack. When there is a crack, the time is 0.2175 ms, which is 0.305 ms (58.4%) earlier than when there is no crack. The results also illustrate the effect of cracks on the stress field of the surrounding rock of the tunnel. This provides theoretical support for predicting the failure area of similar projects.

5 Conclusions

Fractured tunnel rock masses often experience disturbances due to dynamic loads from various directions, which strongly affect the stability of the surrounding rock. To understand the fracture patterns near a tunnel under dynamic loads when cracks are present, the OCT model was adopted in this paper. Physical experiments and AUTODYN numerical simulations were carried out. By changing different azimuths of the tunnel to achieve different impact load directions, the following conclusions were finally obtained:

- (1) During crack propagation around the tunnel, the crack velocity decreases, then increases, and finally decreases again. The CIT is approximately consistent with increasing incident angle, and cracking is most likely to occur under the $\pm 45^\circ$ condition.
- (2) When subjected to an impact load, the prefabricated crack begins to initiate first and bond to the incident side of the tunnel except at an angle of $a = 45^\circ$ which is formed by the overlapping of the crack propagated by the prefabricated crack and the crack generated at the bottom of the incident side of the tunnel. Initially, the prefabricated crack develops as a mode I crack. As the crack propagates, it exhibits tensile failure behaviour for cases $a = 0^\circ, 30^\circ, -30^\circ, \text{ and } 90^\circ$. When $a = -90^\circ$, mixed tensile–shear failure occurs. At other angles, the cracks predominantly undergo shear failure.

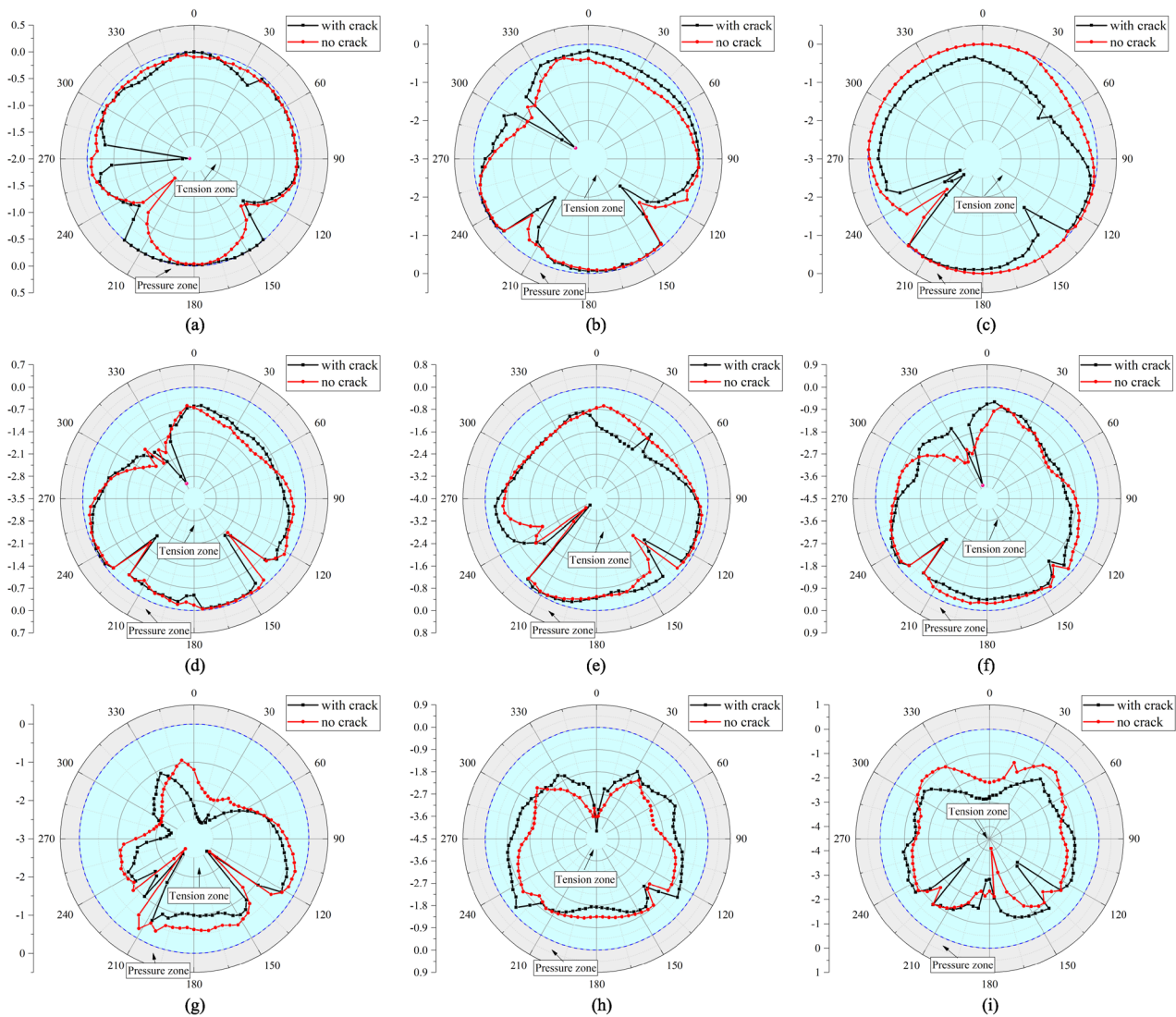


Fig. 14 DSCFs of a tunnel structure under various impact orientations. (a) 0° , (b) 30° (c) -30° , (d) 45° , (e) -45° , (f) 60° , (g) -60° , (h) 90° , and (i) -90°

(3) The damage level of the rock surrounding the tunnel varies with the impact load direction. Higher circumferential stress levels increase the likelihood of damage occurring. In terms of crack propagation, the preexisting crack tends to deflect towards the nearest corner of the tunnel for angles such as $a = -30^\circ$, -45° , and -60° . However, for other angles, the crack propagates to the middle of the tunnel. Concentrated damage on

the transmission side of the tunnel mainly occurs at the bottom corner and the middle segments.

(4) When there are cracks around the tunnel, the DSCF is on average 6.19 times greater than when there are no cracks, with a maximum difference of 20 times. Additionally, the presence of cracks causes fluctuations in the stress distribution of the rock surrounding the tunnel. Under dynamic loads, cracks will lead to an earlier onset of rock vibration.

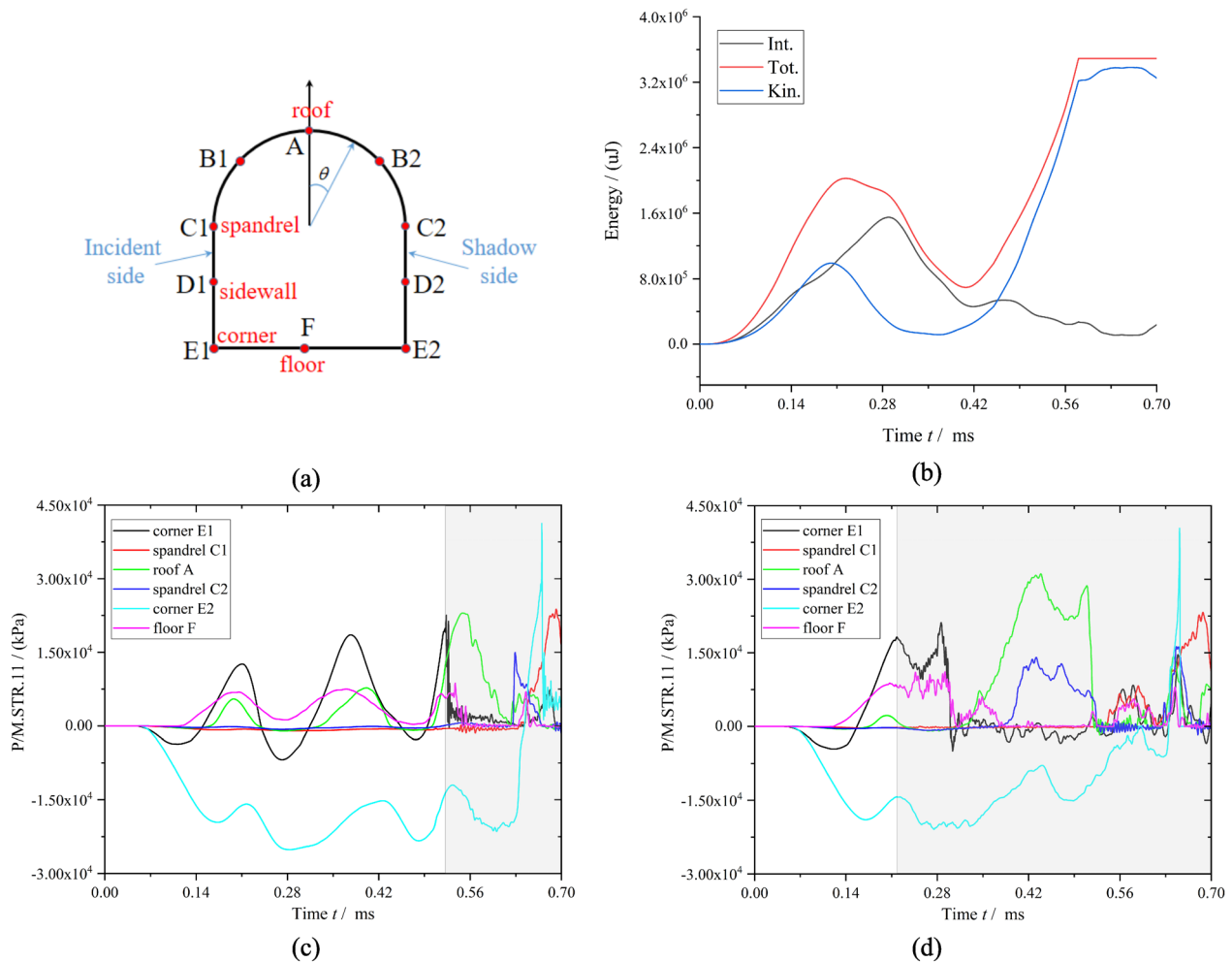


Fig. 15 Time-history curve of the stress wave in the rock surrounding the tunnel: **(a)** stress distribution around the tunnel in polar coordinates; **(b)** input of the internal energy, total energy, and kinetic energy of the structure; **(c)** stress variation in the surrounding rock of the tunnel

at monitoring points without crack influence, and **(d)** stress variation in the surrounding rock of the tunnel at monitoring points with crack influence

Acknowledgements This work was financially supported by the National Natural Science Foundation of China (Grant Nos. 52078467, 52204104, 12272247, and 52374078); Research Development Fund of Zhejiang A&F University (Grant No. 2023LFR026); National Science Foundation of Zhejiang Province (Grant No. LHZ21E09001). The authors sincerely thank Ting Ai at the Structural Laboratory of Civil Engineering in Sichuan University for her valuable assistance.

Funding This work was funded supported by National Natural Science Foundation of China, 52078467, Peng Ying, 52204104, Peng Ying, 12272247, Peng Ying, 52374078, Peng Ying, Research Development Fund of Zhejiang A&F University, 2023LFR026, Peng Ying, National Science Foundation of Zhejiang Province, LHZ21E09001, Peng Ying.

Data Availability No data were used for the research described in the article.

Declarations

Conflict of interest The authors have no relevant financial or non-financial interests to disclose.

References

- Areias P, Rabczuk T (2017) Steiner-point free edge cutting of tetrahedral meshes with applications in fracture. *Finite Elem Anal Des* 132:27–41
- Areias P, Rabczuk T, Dias-da-Costa D (2013) Element-wise fracture algorithm based on rotation of edges. *Eng Fract Mech* 110:113–137
- Areias P, Msekh MA, Rabczuk T (2016) Damage and fracture algorithm using the screened poisson equation and local remeshing. *Eng Fract Mech* 158:116–143

- Aydin A (2009) ISRM suggested methods for determination of the schmidt hammer rebound hardness: revised version. *Int J Rock Mech Min Sci* 46:627–634
- Bruneau G, Tyler DB, Hadjigeorgiou J, Potvin Y (2003) Influence of faulting on a mine shaft—a case study: part I—background and instrumentation. *Int J Rock Mech Min Sci* 40:95–111
- Cai M, Kaiser PK (2005) Assessment of excavation damaged zone using a micromechanics model. *Tunn Undergr Space Technol* 20:301–310
- Cai M, Kaiser PK, Tasaka Y, Maejima T, Morioka H, Minami M (2004) Generalized crack initiation and crack damage stress thresholds of brittle rock masses near underground excavations. *Int J Rock Mech Min Sci* 41:833–847
- Chen YM (1975) Numerical computation of dynamic stress intensity factors by a Lagrangian finite-difference method (the HEMP code). *Eng Fract Mech* 7:653–660
- Chen H, Fan X, Lai H, Xie Y, He Z (2019) Experimental and numerical study of granite blocks containing two side flaws and a tunnel-shaped opening. *Theor Appl Fract Mech* 104:102394
- Feng F, Li X, Rostami J, Li D (2019) Modeling hard rock failure induced by structural planes around deep circular tunnels. *Eng Fract Mech* 205:152–174
- Foster JT, Chen W, Luk VK (2011) Dynamic crack initiation toughness of 4340 steel at constant loading rates. *Eng Fract Mech* 78:1264–1276
- Fraldi M, Guarracino F (2010) Analytical solutions for collapse mechanisms in tunnels with arbitrary cross sections. *Int J Solids Struct* 47:216–223
- Freund LB (1990) *Dynamic fracture mechanics: index*. Cambridge University Press
- Gao F, Kaiser PK, Stead D, Eberhardt E, Elmo D (2019) Strainburst phenomena and numerical simulation of self-initiated brittle rock failure. *Int J Rock Mech Min Sci* 116:52–63
- Gong F, Wuxing W, Tianbin L, Xuefeng S (2019) Experimental simulation and investigation of spalling failure of rectangular tunnel under different three-dimensional stress states. *Int J Rock Mech Min Sci* 122:104081
- Hamdia KM, Silani M, Zhuang X, He P, Rabczuk T (2017) Stochastic analysis of the fracture toughness of polymeric nanoparticle composites using polynomial chaos expansions. *Int J Fract* 206:215–227
- Huang F, Zhu H, Xu Q, Cai Y, Zhuang X (2013) The effect of weak interlayer on the failure pattern of rock mass around tunnel—scaled model tests and numerical analysis. *Tunn Undergr Space Technol* 35:207–218
- Jia P, Tang CA (2008) Numerical study on failure mechanism of tunnel in jointed rock mass. *Tunn Undergr Space Technol* 23:500–507
- Kaiser PK, Cai M (2012) Design of rock support system under rockburst condition. *J Rock Mech Geotech Eng* 4:215–227
- Li H, Wong LNY (2012) Influence of flaw inclination angle and loading condition on crack initiation and propagation. *Int J Solids Struct* 49:2482–2499
- Li M, Zhu Z, Liu R et al (2018) Study of the effect of empty holes on propagating cracks under blasting loads. *Int J Rock Mech Min Sci* 103:186–194
- Li J, Hu J, Zhao Y, Zhao Z, Chen Y, Li B (2024a) Failure characteristics of tunnel under the true triaxial condition: role of a prefabricated flaw. *Theoretical Appl Fract Mech* 130:104327
- Li X-F, Du K, Zhou J, Yin ZQ (2024b) Failure behaviors of square-tunnel-structured rock specimens under various inclined boundary stress conditions. *Eng Fail Anal* 157:107888
- Liu R, Zhu Z, Li Y, Liu B, Wan D, Li M (2020) Study of rock dynamic fracture toughness and crack propagation parameters of four brittle materials under blasting. *Eng Fract Mech* 225:106460
- Luo Y, Gong F, Liu D, Wang S, Si X (2019) Experimental simulation analysis of the process and failure characteristics of spalling in D-shaped tunnels under true-triaxial loading conditions. *Tunn Undergr Space Technol* 90:42–61
- Malmgren L, Saiang D, Töyrä J, Bodare A (2007) The excavation disturbed zone (EDZ) at Kiirunavaara mine, Sweden—by seismic measurements. *J Appl Geophys* 61:1–15
- Nasehi MJ, Mortazavi A (2013) Effects of in-situ stress regime and intact rock strength parameters on the hydraulic fracturing. *J Petrol Sci Eng* 108:211–221
- Saiang D (2010) Stability analysis of the blast-induced damage zone by continuum and coupled continuum–discontinuum methods. *Eng Geol* 116:1–11
- Suorinen FT, Tannant DD, Kaiser PK (1999) Determination of fault-related sloughage in open stopes. *Int J Rock Mech Min Sci* 36:891–906
- Tao M, Ma A, Zhao R, Hashemi SS (2020) Spallation damage mechanism of prefabricated elliptical holes by different transient incident waves in sandstones. *Int J Impact Eng* 146:103716
- Viktorov IA (1967) Rayleigh and lamb wave—physical theory and applications. *Ultrason Technol*. <https://doi.org/10.1007/978-1-4899-5681-1>
- Vu-Bac N, Lahmer T, Zhuang X, Nguyen-Thoi T, Rabczuk T (2016) A software framework for probabilistic sensitivity analysis for computationally expensive models. *Adv Eng Softw* 100:19–31
- Wang M, Zhu ZM, Dong YQ, Zhou L (2017) Study of mixed-mode I/II fractures using single cleavage semicircle compression specimens under impacting loads. *Eng Fract Mech* 177:33–44
- Weng L, Li XB, Taheri A, Wu QH, Xie XF (2017) Fracture evolution around a cavity in brittle rock under uniaxial compression and coupled static–dynamic loads. *Rock Mech Rock Eng* 51:531–545
- Weng L, Wu Z, Li X (2018) Mesodamage characteristics of rock with a pre-cut opening under combined static–dynamic loads: a nuclear magnetic resonance (NMR) investigation. *Rock Mech Rock Eng* 51:2339–2354
- Wong LNY, Li H (2013) Numerical study on coalescence of two preexisting coplanar flaws in rock. *Int J Solids Struct* 50:3685–3706
- Yao W, Xia K (2019) Dynamic notched semi-circle bend (NSCB) method for measuring fracture properties of rocks: fundamentals and applications. *J Rock Mech Geotech Eng* 11:1066–1093
- Yi C, Zhang P, Johansson D, Nyberg U (2014) Dynamic response of a circular lined tunnel with an imperfect interface subjected to cylindrical P-waves. *Comput Geotech* 55:165–171
- Ying P, Zhu ZM, Wang F, Wang M, Niu C, Zhou L (2019) The characteristics of dynamic fracture toughness and energy release rate of rock under impact. *Measurement* 147:106884
- Ying P, Zhu Z, Ren L, Deng S, Niu C, Wan D, Wang F (2020) Deterioration of dynamic fracture characteristics, tensile strength and elastic modulus of tight sandstone under dry-wet cycles. *Theoret Appl Fract Mech* 109:102698
- Zhang XP, Wong L (2014) Displacement field analysis for cracking processes in bonded-particle model. *Bull Eng Geol Environ* 73:13–21
- Zhang QB, Zhao J (2014) Quasi-static and dynamic fracture behaviour of rock materials: phenomena and mechanisms. *Int J Fract* 189:1–32
- Zhang PS, Zhao CY, Li TH, Hou JQ, Zhang R (2021) Experimental study on wave velocity variation and energy evolution of red sandstone during triaxial loading process. *Chin J Rock Mech Eng* 40:1369–1382
- Zhao H, Liu C, Huang G, Yu B, Liu Y, Song Z (2020a) Experimental investigation on rockburst process and failure characteristics in trapezoidal tunnel under different lateral stresses. *Constr Build Mater* 259:119530
- Zhao Y, Bi J, Zhou X-P (2020b) Quantitative analysis of rockburst in the surrounding rock masses around deep tunnels. *Eng Geol* 273:105669
- Zhu ZM, Mohanty B, Xie HP (2007) Numerical investigation of blasting-induced crack initiation and propagation in rocks. *Int J Rock Mech Min Sci* 44:412–424
- Zhu ZM, Li YX, Xie J, Liu B (2015) The effect of principal stress orientation on tunnel stability. *Tunn Undergr Space Technol* 49:279–286

Publisher's Note Springer Nature remains neutral with regard to jurisdictional claims in published maps and institutional affiliations.

Springer Nature or its licensor (e.g. a society or other partner) holds exclusive rights to this article under a publishing agreement with the

author(s) or other rightsholder(s); author self-archiving of the accepted manuscript version of this article is solely governed by the terms of such publishing agreement and applicable law.